Ultrastable Molybdenum Disulfide-Based Electrocatalyst for Hydrogen Evolution in Acidic Media

Yunxing Zhao[1,2,3],† Jeemin Hwang[4],† Michael Tang[5], Hoje Chun[4], Xingli Wang[6], Hu Zhao[2], Karen Chan[7], Byungchan Han[4],* Pingqi Gao[8],** Hong Li[2,6,9]***

[1]Ningbo Institute of Material Technology and Engineering, Chinese Academy of Sciences, Ningbo 315201, China
[2]School of Mechanical and Aerospace Engineering, Nanyang Technological University, 639798, Singapore
[3]University of Chinese Academy of Sciences, Beijing 100049, China
[4]Department of Chemical and Biomolecular Engineering, Yonsei University, Seoul 03722, Republic of Korea
[5]SUNCAT Center for Interface Science and Catalysis, Department of Chemical Engineering, Stanford University, California 94305, USA
[6]CINTRA CNRS/NTU/THALES, UMI 3288, Research Techno Plaza, 637553, Singapore
[7]Catalysis Theory Center, Department of Physics, Technical University of Denmark, Lyngby, Denmark 2820
[8]School of Materials, Sun Yat-sen University, Guangzhou 510275, China
[9]Centre for Micro-/Nano-electronics (NOVITAS), School of Electrical and Electronic Engineering, Nanyang Technological University, 639798, Singapore
†equal contribution
Corresponding author. *Byungchan Han: bchan@yonsei.ac.kr; **Pingqi Gao: gaopq3@mail.sysu.edu.cn; ***Hong Li: ehongli@ntu.edu.sg Tel: +0065 6790 5519

ABSTRACT

Despite the incredible success in reducing the overpotential of nonprecious catalysts for acidic hydrogen evolution reaction (HER) in the past few years, the stability of most platinum-free electrocatalysts is still poor. Here, we report an ultrastable electrocatalyst for acidic HER based on two-dimensional (2D) molybdenum disulfide (MoS_2) doped with trace amount of palladium (<5 μg cm^{-2}), which creates sulfur vacancies (S-vacancies). The optimized catalyst shows stable operation over 1000 h at 10 mA cm^{-2} with overpotential of 106 mV. The MoS_2 catalyst is stabilized on a defective vertical graphene support, where the strong interaction at the 2D-2D interface increases the adhesion between the catalyst and the support. Palladium (Pd) doping generates rich sulfur vacancies in MoS_2 that have a twofold role: (1) increasing hydrogen adsorption energy, which enhances activity; and (2) further increasing the adhesion between graphene support and defective MoS_2, and thus enhancing stability. Complementary theoretical studies reveal the reaction pathways for substitutional doping, where the Mo-vacancy sites are prior to be doped by Pd. Our work thus offers a strategy for making stable, efficient, and earth-abundant HER catalysts with strong potential to replace platinum for PEM electrolysis.

Keywords: vertical graphene network; MoS_2 electrocatalyst; 2D-2D interface; acidic HER; Palladium doping mechanism; long-term stability

1. Introduction

Hydrogen fuel is one of the most promising energy carriers for a sustainable energy future because it can address both energy issue (high energy density) and environment concern (free of carbon emission).[1-4] However, hydrogen is clean and renewable only when it is made from water electrolysis, instead of fossil fuel. A truly sustainable energy future can be achieved if hydrogen is made from water electrolysis that is driven by renewable energy sources such as wind or solar.[5] However, these renewable energy sources are usually intermittent and uncontrollable,[6] which is only compatible with water electrolysis technology that can operate dynamically in a wide potential window. To this end, proton-exchange membrane (PEM) electrolysis,[7] which has high partial load capability, is the most promising technology that could become truly sustainable when it is driven by renewable energy sources. Nevertheless, commercial PEM electrolysis relies heavily on precious catalysts including platinum (Pt) and ruthenium/iridium.[8] Hence, developing Pt-free catalysts or catalysts with minimized Pt loading is of great significance for large-scale production of hydrogen through PEM electrolysis technology driven by renewable energy sources.

Molybdenum disulfide (MoS_2) is regarded as one of the most promising alternatives to Pt in PEM electrolysis for hydrogen evolution reaction (HER).[9, 10] There are three types of active sites on MoS_2 HER catalyst reported to date including edge-sites,[10] 1*T*-phase,[11] and sulfur vacancies (S-vacancies) in the basal plane of 2*H* phase.[12, 13] Edge-sites are, however, abundant only when MoS_2 nanoparticles are extremely small, and it is a challenge to distribute tiny nanoparticles on a catalyst

support in a uniform fashion.[14] The 1*T*-phase is active but metastable.[15] S-vacancies on the basal plane of 2*H*-phase MoS_2 are very abundant, and strained S-vacancies have shown an unprecedented turnover frequency.[12, 16] Nevertheless, three major challenges remain: (1) poor stability under acidic HER conditions, (2) the lack of methods to introduce S-vacancies in bulk MoS_2, and (3) the high sensitivity of the HER activity to the concentration of S-vacancies (or %S-vacancy). The first challenge arises from the tradeoff between the activity and stability of the catalyst, similar to most acidic HER electrocatalysts.[17] The long-term stability of nonprecious HER electrocatalysts in acidic media remains poor (most of them show no more than 100-h stability at 10 mA cm^{-2}) [18, 19], though the catalytic activity has been greatly improved to be close to that of Pt.[20-22] Techniques to increase the stability without compromising the high activity of Pt-free HER electrocatalyst is therefore critical towards their wide adoption.

The highly active S-vacancies can be created in MoS_2 by mild argon plasma etching,[23] electrochemical reduction,[24] or metal substitutional doping.[25, 26] The argon plasma etching does not work for bulk MoS_2 (*e.g.*, powder form as in commercial catalyst) due to the anisotropic nature of plasma etching. On the other hand, the electrochemical reduction method is sensitive to substrate, and has poor controllability in nanostructured MoS_2 because electrochemical desulfurization depends highly on whether the reduction potential can be effectively applied onto the MoS_2 surface. In contrast, the metal substitutional doping method shows great promise to introduce S-vacancies into bulk MoS_2 in a controllable way. However, the detailed reaction

mechanisms are unclear.[25]

Herein, we address the aforementioned challenges in two ways: (1) we stabilize the 2D MoS_2 electrocatalyst on 2D defective graphene support by forming a stable 2D-2D interface, and (2) we introduce S-vacancies using optimized Pd substitutional doping. The optimized catalyst shows low overpotential close to 100 mV at 10 mA cm^{-2}, and its superior performance remains stable for over 1000 h in acidic media (0.5 M sulfuric acid). The catalyst with 3D open structure also offers high current density with excellent stability (over 180 h at 80 mA cm^{-2}). To the best of our knowledge, this combination of low overpotential, high current density, and superior stability in acidic media far exceeds the performance of previously reported MoS_2-based HER electrocatalysts.[27]

2. Experimental

2.1. Samples preparation

Ammonium tetrathiomolybdate [$(NH_4)_2MoS_4$] and $PdCl_2$ were purchased from Sigma-Aldrich, and DMF (N, N-dimethylformamide) was purchased from Sinopharm Chemical Reagent Co., Ltd., and all chemicals were used as received. Carbon fiber paper (CFP, TGP-H-060, Toray, Japan) served as substrate with 4×4 cm^2 in size, and it was ultrasonically cleaned by acetone, ethanol, and deionized water for 10minuts, respectively. For the growth of vertical graphene， microwave plasma enhanced chemical vapor deposition (MPECVD) equipment was adopted with CH_4 and H_2 as reaction gases and Argon as carrier gas. The flow rates of CH_4, H_2, Ar were 30 sccm,

0.9 slm and 21.5 slm, respectively. And the deposition process was carried out at an input plasma power of 18kW for 3 min, as well as a fixed pressure of 800 Pa. Solvothermal method was used for the hybrid of MoS_2 and vertical graphene. In detail, 30 mg $(NH_4)_2MoS_4$ was dissolved into 30 mL dry DMF before the solution was transformed into 45 ml Teflon-sealed autoclave, then a piece of CFP covered with vertically graphene on the surface was putted and the autoclave was heated at 200℃ for 15 hours to give VGN@MoS_2. For the Pd doping, VGN@MoS_2 was immersed into $PdCl_2$ solution with different weight concentrations of $PdCl_2$ powder to water (0.2‰, 0.1‰, 0.05‰, and 0.025‰) at 50℃ for 2 hours. Perfect 2*H*-MoS_2 flakes on Si/SiO_2 wafer were grown by chemical vapour deposition (CVD), with molybdenum trioxide (MoO_3) and sulphur (S) powder as sources in a tube furnace.[12] The Pd doped CVD MoS_2 sample for microRaman characterization was prepared by soaking the sample in 0.2‰ $PdCl_2$ solution at 50℃ for 2 hours.

2.2. Characterizations

The morphologies were characterized via field-emission scanning electron microscopy (FESEM; Thermo scientific, Verios G4 UC and Hitachi, S-4800) and transmission electron microscopy (TEM; Themo Fisher, Talos F200x, 200 kV). Energy dispersive X-Ray spectrometry (EDS) analyses were conducted by the same TEM equipment equipped with a four-quadrant FEI Super-X detector, and Thermo scientific Verios G4 UC FESEM equipment equipped with an Oxford instrument X-max 50 EDX detector. X-ray diffraction (XRD; Bruker D8 Advance Davinci) was used to investigate the structure information using Cu Kα (λ = 1.5406 Å) radiation. Raman spectra were

collected by using a Renishaw in Via reflex spectrometer at an excitation wavelength of 532 nm at room temperature. And X-ray photoelectron spectroscopy (XPS) information was recorded by an AXIS ULTRA DLD Kratos system with Al Kα X-ray source (hν = 1486.8 eV). The concentrations of ions were measured by inductively coupled plasma optical emission spectra (ICP-OES, SPECTRO ARCOS Ⅱ, Germany). The samples (4 cm^2) were dissolved in concentrated nitric acid (10 mL) under heating for 2h firstly before further washed sufficiently with aqueous ammonia, and all solution was transferred to a 25 ml volumetric flask for quantification with DI water. Raman characterization was performed using a WITEC alpha300 R confocal Raman system in air ambient environment. The excitation laser line was 532 nm and the intensity was set as low as 1.4 mW to avoid heating effect while the Raman peaks remained prominent. Before the characterization, the system was calibrated with Si peak at 520 cm^{-1} to keep the measurement consistent. The Raman emission was collected by an Olympus 100 × objective (N.A. = 0.8) and dispersed by a grating of 1800 lines mm^{-1}. For each spot in the Raman mapping, the moving step of the piezo-stage was set to 250 nm with an integration time of 0.5 s.

2.3. Electrochemical measurements

Electrochemical measurements excluding stability test were carried out on one electrochemical workstation (Biologic VSP-300, France), and stability tests were recorded on another instrument (CHI 660E, China). All LSV (linear sweep voltammetry) tests were conducted in a three-electrode cell in 0.5 M H_2SO_4 solution with the potential sweep rate at 2 mV s^{-1}. Electrochemical impedance spectroscopy (EIS)

was carried out on the open-circuit potential in the frequency range from 10^5 Hz to 0.1 Hz. A saturated Ag/AgCl electrode served as a reference electrode and the VGN@Pd_x-MoS_2 served as working electrode directly, and all the potentials were referenced to the reversible hydrogen electrode (RHE) with 85% iR correction (automatic compensation of the iR drop in three-electrode systems by an electrochemical workstation, where the series resistance R_s was obtained under open-circuit voltage prior to starting the experiments) for LSV curves and full iR correction (manual iR compensation, where R_s was obtained from EIS result under open-circuit voltage) for V-t curves. The measured potentials were converted to RHE using the equation: E(RHE) = E(Ag/AgCl) + 0.0591 × pH + 0.197 V. The electrochemical double layer capacitance (C_{dl}) was measured by cyclic voltammetry (CV) curves in non-Faradaic region with different scan rates of 10, 20, 40, 60, 80, 100 mV s^{-1}. A piece of carbon fiber paper served as counter electrode during stability tests and it was replaced by a new one every 100 hours, and Pt wire was chosen as counter electrode for the other measurements.

2.4. DFT Simulations

First-principles density functional theory (DFT) calculations were performed using the Vienna Ab-initio Simulation Package (VASP).[28] The interactions with core electrons were simulated by the Projector Augmented Wave (PAW) method[29] and the exchange-correlation energy was described with the generalized gradient approximation (GGA)[30] using the revised Perdew-Burke-Ernzerhof (RPBE) functional.[31] Spin-polarization effects were considered and van der Waals (vdW) interactions were described by the DFT-D2 method of Grimme.[32] Plane wave basis

functions were expanded with cut-off energy of 520 eV and k-points were sampled using 3 × 3 × 1 for the structural relaxations. Calculations were continued until the energy and force converged within 1×10^{-6} eV and 0.02 eV $Å^{-1}$, respectively. To prevent interactions among the image clusters, a vacuum of 15 Å perpendicular to the surface was inserted.

The defect (E_{defect}) and doping (E_{doping}) formation energies were calculated as

$$E_{\mathrm{defect}} = E_{\mathrm{defected}} - E_{\mathrm{pr}} + \mu_{\mathrm{S/Mo}} \quad \text{(eq 1)}$$

$$E_{\mathrm{doping}} = E_{\mathrm{doped}} - E_{\mathrm{pr}} - E_{\mathrm{Pd}} \quad \text{(eq 2)}$$

where, E_{defected}, E_{doped}, E_{pr} and $\mu_{\mathrm{S/Mo}}$ are, respectively, the total energy of system with atomic defect(s), dopant(s), pristine slab, and chemical potential of S and Mo. The chemical potential of Mo satisfies the equation $\mu_{\mathrm{MoS_2}} = \mu_{\mathrm{Mo}} + 2\mu_{\mathrm{S}}$ under thermodynamic equilibrium, where $\mu_{\mathrm{MoS_2}}$ is the chemical potential of MoS_2 in a pristine sheet and the S chemical potential was obtained as total energy of bulk alpha-S divided by the number of atom.[33] The energy of Pd (E_{Pd}) was calculated as the atomic energy of Pd in $PdCl_2$.

The Gibbs free energy of hydrogen adsorption (ΔG_H) was defined as

$$\Delta G_{\mathrm{H}} = \left(E_{\mathrm{H^*}} - E_{\mathrm{pr}} - \frac{1}{2}E_{\mathrm{H_2}}\right) + \Delta E_{\mathrm{ZPE}} - T\Delta S \quad \text{(eq 3)}$$

where, $E_{\mathrm{H^*}}$ is the energy of the slab with H* adsorbed, and $E_{\mathrm{H_2}}$ is the hydrogen gas reference. The asterisk (*) denotes the adsorption site of hydrogen atom. Also, ΔE_{ZPE}, T and ΔS refer to the zero-point energy corrections, temperature and the entropy difference between the gas and adsorbed phase.[34]

Relative energetic phase stability between the 2*H* and 1*T* structure (ΔE) was evaluated

as

$$\Delta E = E(2H) - E(1T) \quad \text{(eq 4)}$$

where E(2*H*) and E(1*T*) mean total energy of catalysts with Pd-doping induced S-vacancy in 2*H*- and 1*T*-phase, respectively. The negative (positive) ΔE indicates that the 2*H* (1*T*) structure is more stable.

DFT calculations for adsorption between MoS_2 and VGN were performed using the Atomic Simulation Environment (ASE) with Quantum Espresso code using plane-wave ultrasoft pseudopotentials following our former reported methods,[35] where single graphene layer and single MoS_2 layer are chosen for study their interface interaction.

The adsorption energy of MoS_2 on the graphene support was defined by:

$$\Delta E(ads) = \big(E(\mathrm{MoS_2} + \mathrm{graphene}) - E(\mathrm{MoS_2}) - E(\mathrm{graphene})\big)/Nc \quad \text{(eq 5)}$$

Where the adhesion energy of MoS_2 on the support was normalized to the number of carbon atoms N_C in the supercell.

3. Results and Discussion

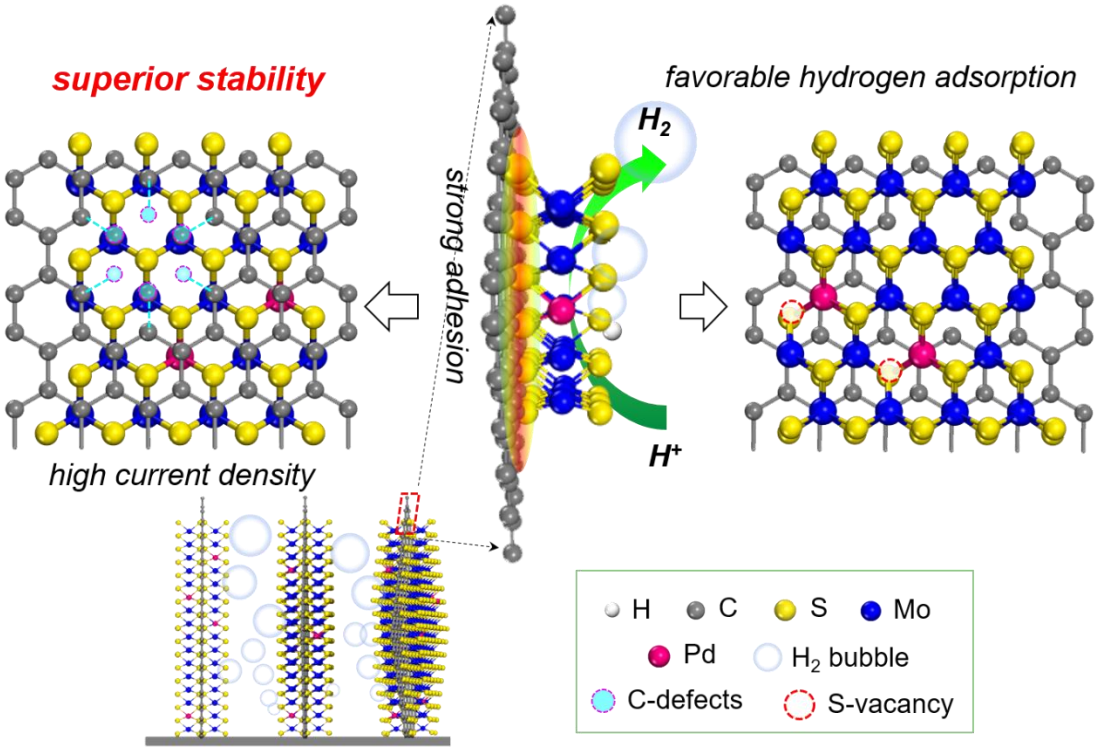

Fig. 1. Schematic illustration of hydrogen evolution catalyzed by palladium-doped MoS_2 anchored on vertical graphene. The substitutional palladium doping induced sulfur vacancies optimize the hydrogen adsorption energy, and thus boost the catalytic activity. The open network and high surface area of vertical graphene network lead to high electrochemical capacitance. Most importantly, the defective graphene and doped MoS_2 interacts strongly at their interface, resulting in the superior stability of the catalyst. The blue, yellow, pink, grey and white balls represent Mo, S, Pd, C and H atoms, respectively. The solid and open dotted circles label the carbon defects (C-defects) in graphene and sulfur vacancy (S-vacancy) in doped MoS_2, respectively. The blue circles with various sizes show the hydrogen bubbles.

The cathode structure is illustrated in Fig. 1, where the catalyst (MoS_2 with S-vacancies) is supported on a vertical graphene network (VGN) substrate. The S-

vacancies are introduced by Pd substitutional doping, where a Pd atom replaces a Mo atom in the lattice. Such a cathode geometry has a few advantages (1) stable 2D-2D interface with minimum surface energy stabilizes the 2D MoS_2 electrocatalyst on 2D graphene, (2) defects in graphene arising from the mesoplasma during VGN synthesis enhance the catalyst-support interaction and further increase the stability, (3) VGN support has an open structure that allows efficient ion transport and large catalyst-electrolyte contact area, and (4) high electrical conductivity of VGN due to high synthesis temperature (900 ^oC) minimizes the Ohmic loss and further decreases overpotential. The brief fabrication process of the cathode is as follows (see Methods for details). Firstly, VGN was grown on carbon fiber paper (CFP) in mesoplasma-enhanced chemical vapor deposition (MPECVD) equipment. The growth process was carried out with an input plasma power of 18 kW for 3 min at 900 ^oC. The as-grown VGN consists of a network of standing defective graphene flakes with many open pores (Fig. S1). The VGN coated CFP offers a perfect catalyst support with hierarchical open structure, excellent electrical conductivity, high-surface area, and chemically active surface. Then, MoS_2 was grown on the support using solvothermal method followed by Pd doping, which was performed by simply soaking the VGN@MoS_2 sample in palladium chloride ($PdCl_2$) solution. The morphology analysis from scanning electron microscopy (SEM) images (Fig. 2a and 2b, Fig. S1) indicates that VGN@MoS_2 and VGN@$Pd_{0.2}$-MoS_2, where the subscript 0.2 denotes the initial concentration of $PdCl_2$ in permillage, have vertical structure with ample open pores inheriting from VGN. Such an open vertical structure facilitates transport of electrolyte to inner space of the

complex geometry, resulting in large contact area between electrolyte and catalyst.

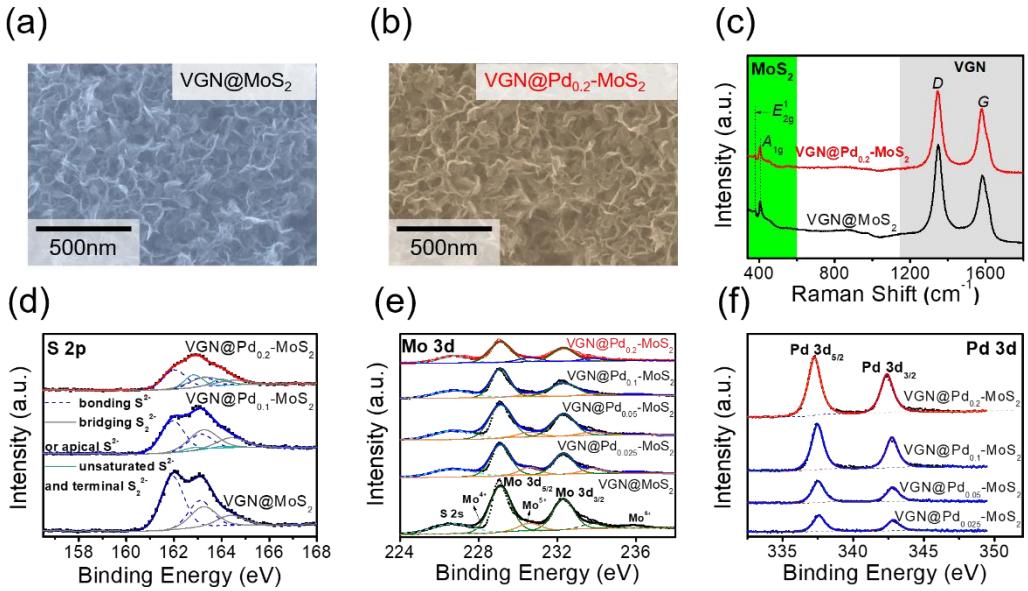

Fig. 2. Catalyst material characterization. SEM images of (a)VGN@MoS_2, and (b)VGN@$Pd_{0.2}$-MoS_2. Scale bars in (a) and (b) are 500 nm. (c) Raman spectra of VGN@$Pd_{0.2}$-MoS_2 and VGN@MoS_2. (d-f) XPS spectra of S 2p, Mo 3d and Pd 3d states, respectively, of VGN@Pd_x-MoS_2, where x varies between 0.2 and 0.025.

It is worth noting that MoS_2 grown on VGN results in thin MoS_2 flakes, as shown in Fig. 2a (see Fig. S1, Fig. S2a for more details), where no obvious MoS_2 cluster is evident, while the direct growth of MoS_2 on CFP (CFP@MoS_2) forms large clusters (Supplementary Fig. S2b). The atomic ratios of S to Mo is ~2.1, indicating the nonstoichiometric MoS_2 growth, and all elements of C, O, Mo, S exhibit uniform distributions in the hybrid VGN@MoS_2 system, as shown in Fig. S2. Transmission electron microscopy (TEM) images further confirm the heterostructure of VGN@MoS_2, as displayed in Supplementary Fig. S3. The translucent nanosheets in Fig. S3a indicate

ultrathin MoS_2 flakes grown on ultrathin graphene. High-resolution TEM (HRTEM) image in Supplementary Fig. S3b reveals that only few-layer-thick MoS_2 (with lattice fringe of 0.66 nm) were grown on graphene layers, indicating VGN limited the growth of MoS_2, also consistent with previous reports[36, 37]. The selected area electron diffraction (SAED, inset of Fig. S3b) pattern suggests the catalyst has poor crystallinity. The element distributions in VGN@$Pd_{0.2}$-MoS_2 (See Fig. S3c for TEM image) were obtained from scanning TEM-energy dispersive X-ray spectroscopy (STEM-EDS) images (Supplementary Fig. S3e and S3f). The results show that different elements including C, S, Mo, Pd have fairly uniform distributions in the entire nanosheet except for minor aggregations of S and Mo elements, which could be caused by folding of MoS_2 flakes. Otherwise, thin-layer MoS_2 and 2D heterostructure of MoS_2 and graphene could still be observed in region of thin flake, as displayed in Fig. S3d.

X-ray powder diffraction (XRD) and Raman spectra were carried out to analyze the structure and crystal information of the hierarchical catalyst. As shown in Supplementary Fig. S4a, no obvious MoS_2 peaks appeared in XRD spectrum, which suggests that MoS_2 flakes have low crystallinity[38], consistent with SAED analysis. The Raman spectra (Fig. 2c) show E_{2g}^1 modes (380 cm^{-1}) and A_{1g} modes (406 cm^{-1}), corresponding to 2*H*-phase MoS_2.[39] The peaks located at G (1348 cm^{-1}) and D (1586 cm^{-1}) indicate defective graphene.[40] Elemental compositions analyses were conducted by XPS for S 2p, Mo 3d, and Pd 3d states. The S 2p mode in Fig. 2d can be deconvoluted into six peaks; those at 162.0 eV and 163.2 eV correspond to 2p of S that forms chemical bonding with Mo or Pd, and 163.3 eV and 164.5 eV belong to S_2^{2-}

related to bridging S_2^{2-} or apical S^{2-}, and the others located at 162.8eV and 164.0 eV may be assigned to unsaturated S^{2-} and terminal S_2^{2-} due to surface reconstruction arising from reaction between MoS_2 and $PdCl_2$.[41-43] It is noted that the significant changes of S peaks represent strong chemically reaction between MoS_2 and $PdCl_2$. Moreover, the unsaturated S^{2-} and terminal S_2^{2-} peaks emerge only when concentration of Pd precursor is more than 0.1‰, *i.e.*, VGN@$Pd_{0.2}$-MoS_2 and VGN@$Pd_{0.1}$-MoS_2. In contrast, these two peaks do not appear in VGN@$Pd_{0.05}$-MoS_2 and VGN@$Pd_{0.025}$-MoS_2 (Supplementary Fig. S4b), demonstrating the quick chemical reaction between MoS_2 and $PdCl_2$ requires higher initial $PdCl_2$ concentration in solution to trigger. As for Mo 3d in Fig. 2e, the peaks at 229.0 eV and 232.3 eV correspond to 3d of Mo^{4+}, and those at 230.6 eV and 233.8 eV belong to Mo^{5+}, which may be ascribed to inadequate reduction from ammonium tetrathiomolybdate precursor or slight oxidation of MoS_2.[44, 45] The peaks located at 337.3 eV and 342.5 eV in Fig. 2f belong to Pd^{2+},[46] and it is noted that no Pd^0 peaks appear after the doping reaction. And as the initial $PdCl_2$ concentration increases from 0.025‰ to 0.2‰, the intensities of Mo peaks decrease gradually while those of Pd increase, suggesting more Mo atoms were replaced by Pd atoms. Considering the lower coordination number of Pd to S atoms,[25] extra sulfur will leach out of MoS_2 lattice after Pd introduction, and the reaction mechanism of this substitutional doping process will be detailed later.

To further quantifying the content of Pd in the doped MoS_2 catalyst, SEM-EDS analysis was employed and the results are displayed in Supplementary Fig. S5, which suggests the weight percentages of Pd in Pd_x-MoS_2 decrease from 7.2%, 3.1%, 1.6%,

to 0.5% for VGN@$Pd_{0.2}$-MoS_2, VGN@$Pd_{0.1}$-MoS_2, VGN@$Pd_{0.05}$-MoS_2, VGN@$Pd_{0.025}$-MoS_2, respectively. The initial $PdCl_2$ concentration in solution, therefore, determined the doping concentration of Pd in catalyst. So the controllable doping of Pd in catalyst can be achieved by adjusting initial $PdCl_2$ concentrations in solution. We further characterized the element concentration by inductively coupled plasma optical emission spectrometry (ICP-OES), which gives the weight percentage of Pd to $Pd_{0.2}$-MoS_2 for VGN@$Pd_{0.2}$-MoS_2 sample as 5.9 % (see Supplementary Fig. S5g for details), which is close to 7.2% obtained from SEM-EDS analysis. In addition, ICP-OES results show that the sum of atomic concentrations of Mo and Pd for VGN@$Pd_{0.2}$-MoS_2 (0.090 mmol L^{-1}) is close to that of Mo in undoped VGN@MoS_2 (0.088 mmol L^{-1}), suggesting the substitutional doping of one Pd to one Mo site. ICP-OES characterizations also give the contents of S element for VGN@MoS_2 (6.071 mg L^{-1}) and VGN@$Pd_{0.2}$-MoS_2 (5.722 mg L^{-1}), which indicate the S concentration dropped by 5.75% after Pd doping process. When VGN is taken into account, the weight percentage of Pd in the catalyst VGN@$Pd_{0.2}$-MoS_2 (CFP substrate is excluded) is ca. 1.4%. This corresponds to a Pd mass loading of 0.005 mg cm^{-2}, 100-200 lower than that of the commercial Pt/C catalyst in PEM electrolyzer (0.5-1 mg cm^{-2}).[7]

Electrochemical tests were carried out to evaluate activity and stability of the catalyst. Linear sweep voltammetry (LSV) curves in Fig. 3a show the increased catalytic performance following the order of VGN@MoS_2, VGN@$Pd_{0.025}$-MoS_2, VGN@$Pd_{0.05}$-MoS_2, VGN@$Pd_{0.1}$-MoS_2, and VGN@$Pd_{0.2}$-MoS_2. VGN@$Pd_{0.2}$-MoS_2 shows the best activity with overpotential of 106 mV at current density of 10 mA cm^{-2},

and those for VGN@$Pd_{0.1}$-MoS_2, VGN@$Pd_{0.05}$-MoS_2, and VGN@$Pd_{0.025}$-MoS_2 are 131 mV, 152 mV, and 200 mV, respectively. VGN@$Pd_{0.2}$-MoS_2 also affords high current density of 100 mA cm^{-2} at overpotential of only 191 mV. The electrochemical impedance spectroscopy (EIS) characterizations indicate increased HER kinetics from VGN@$Pd_{0.025}$-MoS_2 to VGN@$Pd_{0.2}$-MoS_2 (Fig. S6a). The Tafel slopes (Fig. 3b) of VGN@MoS_2 (80 mV dec^{-1}), VGN@$Pd_{0.025}$-MoS_2 (74 mV dec^{-1}), VGN@$Pd_{0.05}$-MoS_2 (67 mV dec^{-1}), VGN@$Pd_{0.1}$-MoS_2 (62 mV dec^{-1}), and VGN@$Pd_{0.2}$-MoS_2 (60 mV dec^{-1}) also suggest the enhanced HER kinetics after doping. The optimal activity of VGN@$Pd_{0.2}$-MoS_2 exceeds those of most Pd and other metal-MoS_2 composite catalysts (see Supplementary Tables S1 and S2 for details). Otherwise, it is noted that all of our samples on VGN support show very small resistances (Supplementary Fig. S6a), suggesting that our VGN has superior electrical conductivity. And remarkably, the electrochemically capacitances C_{dl} (Fig. S6b), which are calculated from double layer area from Supplementary Fig. S6c to S6f, of VGN@$Pd_{0.2}$-MoS_2 (12.5 mF cm^{-2}) and VGN@MoS_2 (11.4 mF cm^{-2}) are significantly larger than those of CFP@$Pd_{0.2}$-MoS_2 (3.9 mF cm^{-2}) and CFP@MoS_2 (3.2 mF cm^{-2}); owning to the highly dispersive open structure and larger contact area between catalyst and electrolyte of VGN catalyst support, which benefits to proton transport efficiently during electrochemical reaction process.

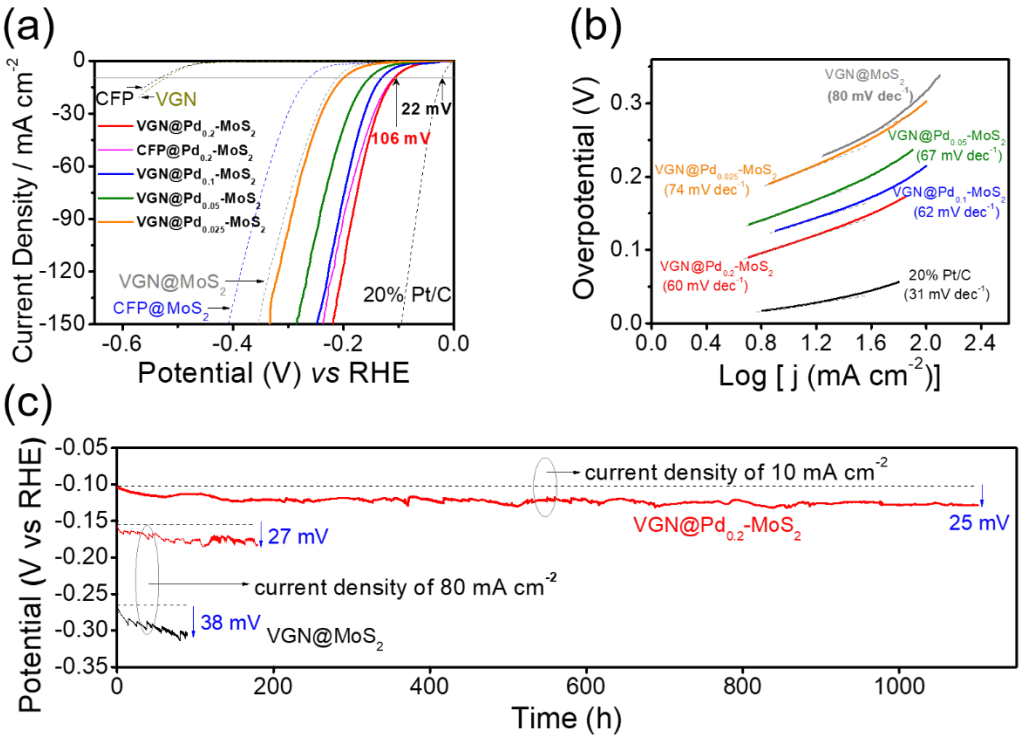

Fig. 3. Electrochemical performances of the catalysts. (a) LSV curves of CFP, VGN, CFP@MoS_2, VGN@MoS_2, VGN@$Pd_{0.025}$-MoS_2, VGN@$Pd_{0.05}$-MoS_2, VGN@$Pd_{0.1}$-MoS_2, CFP@$Pd_{0.2}$-MoS_2, VGN@$Pd_{0.2}$-MoS_2, and 20% Pt/C in 0.5 M H_2SO_4 solution with scan rate of 2 mV s^{-1}. The overpotentials at 10 mA cm^{-2} for VGN@$Pd_{0.2}$-MoS_2 (106 mV) and 20% Pt/C (22 mV) are labelled. (b) Tafel plots of VGN@MoS_2, VGN@$Pd_{0.025}$-MoS_2, VGN@$Pd_{0.05}$-MoS_2, VGN@$Pd_{0.1}$-MoS_2, VGN@$Pd_{0.2}$-MoS_2, and 20% Pt/C. The Tafel slopes of each curve are labelled. (c) Stability test for VGN@$Pd_{0.2}$-MoS_2 at 10 and 80 mA cm^{-2}, respectively. The stability of VGN@MoS_2 at 80 mA cm^{-2} is also shown for comparison. The arrows indicate the overpotential degradation of the catalysts during stability test.

Next, we evaluate the stability of the optimal catalyst VGN@$Pd_{0.2}$-MoS_2. To compare with most HER electrocatalysts in acidic media, we tested the stability at 10

mA cm^{-2}, as shown in Fig. 3c. Strikingly, the catalyst exhibited stable operation up to 1100 h with only 25 mV overpotential decreases with the majority of the degradation occurred in the first 50 h, corresponding to a degradation rate of 23 μV h^{-1}. This superior stability by far outperforms most catalysts operation in acidic environment (see Supplementary Table S3 for detail). This stable operation demonstrates the great potential of our catalyst as a true alternative to Pt-based commercial HER catalyst. Stable operation at high current density, which accelerates the degradation of catalyst, is of great significance to practical application. We thus tested the stability at a relatively high current density of 80 mA cm^{-2}. The overpotential of VGN@$Pd_{0.2}$-MoS_2 degraded by 27 mV after 180-h continuous operation, indicating a degradation rate of 150 μV h^{-1}. Similarly, most of the degradation occurs in the first 60 h. In contrast, VGN@MoS_2 has larger potential drop up to 38 mV after only 90-h continuous operation, indicating a degradation rate of 422 μV h^{-1}. This comparison suggests that Pd doping also increased stability in addition to enhancing activity. The enhanced stability in Pd doped catalyst could be ascribed to its improved corrosion resistance in acidic environment arising from Pd species such as Pd-S and Pd-S-Mo. Moreover, the increased stability could be attributed to the increased adhesion at the MoS_2-VGN interface due to S-vacancies, as will be detailed later. SEM images in Fig. S7 show the surface morphology becomes rougher for the electrode VGN@$Pd_{0.2}$-MoS_2 after 1100-hour continuous operation, due to possible unstable Pd precipitation. XPS further reveals the changes of composites, as displayed in Fig. S7g-S7i, where Mo element shows negligible change while Pd element undergoes partial reduction into zero valence

state, and those bridging S_2^{2-}, apical S^{2-}, unsaturated S^{2-} or terminal S_2^{2-} of S element are hardly observed. Noting that the Pd particles or Pd/C need higher overpotential (>180 mV) to achieve 10 mA cm^{-2} [25, 47, 48]; and thus the remaining Pd with higher valence state and the associated S-vacancy in MoS_2 still afford the stable activity as observed. Even longer stability test may be needed to observe obvious degradation.

We employed density functional theory (DFT) calculation to elucidate the mechanism of Pd doping. Fig. 4a presents a potential energy surface diagram showing three pathways (black, red and blue curves) of the processes with respect to the pristine MoS_2 surface (see Method). In path 1 (the black curve), the reaction begins with Mo-vacancy formation (uphill step ①: +4.81 eV) followed by Pd doping on the Mo-vacancy site (downhill step ②: -3.05 eV), and then ends up with creation of a S-vacancy (uphill step ③: +0.56 eV). In reaction path 2 (the red curve), a Mo- and a S-vacancy form at first (uphill step ①: + 5.35 eV) followed by Pd doping on the Mo-vacancy site (downhill step ③: -3.04 eV). The pathway 3 (the blue curve) starts with the formation of a Mo- and two S-vacancies (uphill step ①: +7.54 eV) followed by Pd doping to the Mo-vacancy site (downhill step ②: -3.61 eV), and then filling one of the two S-vacancy sites (downhill step ③: -1.61 eV). This potential energy surface diagram indicates that a Mo-vacancy formation step is thermodynamically the least spontaneous reaction regardless of the pathway. It is worth noting that once a Pd atom is doped to the Mo-vacancy site, the model systems are substantially stabilized, and the formation of S vacancy becomes energetically favorable. The Pd substitutional doping process is relatively more favorable along path 1 than the others [4.81 eV vs 5.35 (or

7.54) eV]. This suggests that the Pd doping is not able to start directly on basal plane of 2*H* MoS_2 due to the unsurmountable activation energy for removing Mo atom from the MoS_2 lattice. Instead, the doping process may start with Mo-vacancy sites[33] on the grain boundaries[49], defects, or the edge of MoS_2 lattice.

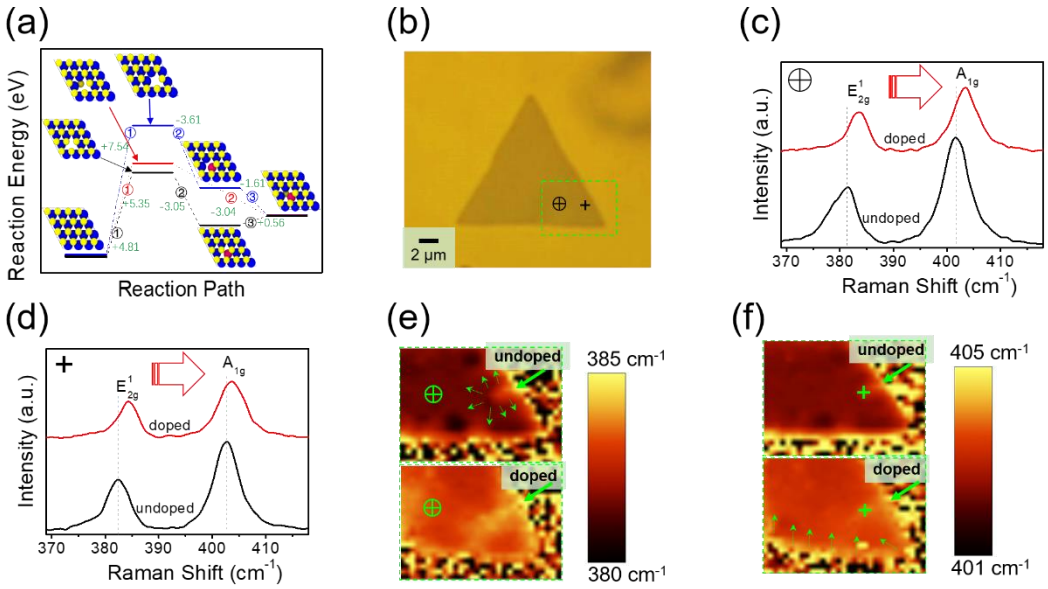

Fig. 4. Pd doping mechanisms and stability of doped MoS_2. (a) The reaction energy vs reaction path. Inset: simulated atomic structures. The initial structure is 2*H*-phase MoS_2 where the blue, pink, and yellow balls represent Mo, Pd and S atoms, respectively. Path 1 (the black pathway) is thermodynamically more favorable due to its lower defect formation energy in comparison with path 2 or 3 (the red and the blue pathway). (b) An optical image of a monolayer CVD MoS_2 flake. (c) Raman spectra taken at point ⊕ in (b) before (lower) and after (upper) Pd doping. (d) Raman spectra taken at point + in (b) before (lower) and after (upper) Pd doping. (e) Raman map of E^1_{2g} position in the area enclosed by the dashed box in (b) before (upper panel) and after (lower panel) doping. The arrows in the upper panel indicate the expanding direction of the defective

site. (f) Raman map of A_{1g} position in the area enclosed by the dashed box in (b) before (upper panel) and after (lower panel) doping. The arrows in the upper panel indicate the change of the edge caused by doping. Insets of (e) and (f) are the color bars.

To find out some insight experimentally, we use a microRaman spectroscopy to monitor the doping process in a perfect 2*H*-MoS_2 flake grown by CVD (see Fig. 4b for optical image of the flake). Raman spectroscopy is very sensitive to the disturbance of electronic structure and chemical composition of monolayer MoS_2 caused by even molecules,[50] thus offers a sensitive tool to investigate the starting of Pd doping process. In order to make a precise comparison, the exciting laser power intensity was kept the same throughout the measurement, and the spectra are normalized with respect to the silicon substrate peak at 520 cm^{-1}. Fig. 4c shows the comparison of the spectrum taken at the point ⊕ (see Fig. 4b) before and after doping process (see Method for details). One can see that both E^1_{2g} and A_{1g} peaks significantly shift towards higher energy (blue shift), which is ascribed to enhancements of both in-plane and out-of-plane lattice vibrations,[39] suggesting the compressive strain has been created after Pd was introduced,[51] possibly owning to the different coordinate environments and bond lengths between Pd-S with Mo-S.[25, 52] As depicted in Fig. 4d, similar blue shift was observed at the defective site (point +), which is indicated by solid arrows in Fig. 4e and 4f. It is worth noting the intensity of the Raman peaks decreases substantially after Pd doping due to the defects (S-vacancies) introduced into the 2*H*-MoS_2 lattice.

An obvious defective site is seen in the mapping of the position of E^1_{2g} peak (Fig.

4e upper panel), though it is not evident in the optical image (Fig. 4b where the dotted square indicates the Raman mapping area). The defective site shows brighter color compared to the rest of the area, indicating blue shift of Raman peaks. Upon Pd doping (Fig. 4e lower panel), the defects expended, as labeled by the dotted arrows. This serves as a direct evidence for the preferential Pd doping starting from defective site. Similar trend was found on the map of A_{1g} peak position (Fig. 4f). A careful comparison shows that the edge of the flake also starts to become more defective (brighter color and more uneven boundary) after Pd doping. This also suggests that Pd doping process most likely starts from the edge site, consistent with the findings from the theory in Fig. 4a. It is worth noting that the actual catalyst made by solvothermal process is much more defective and has less crystallinity than the CVD MoS_2, thus the Pd doping process should occur much easier and faster.

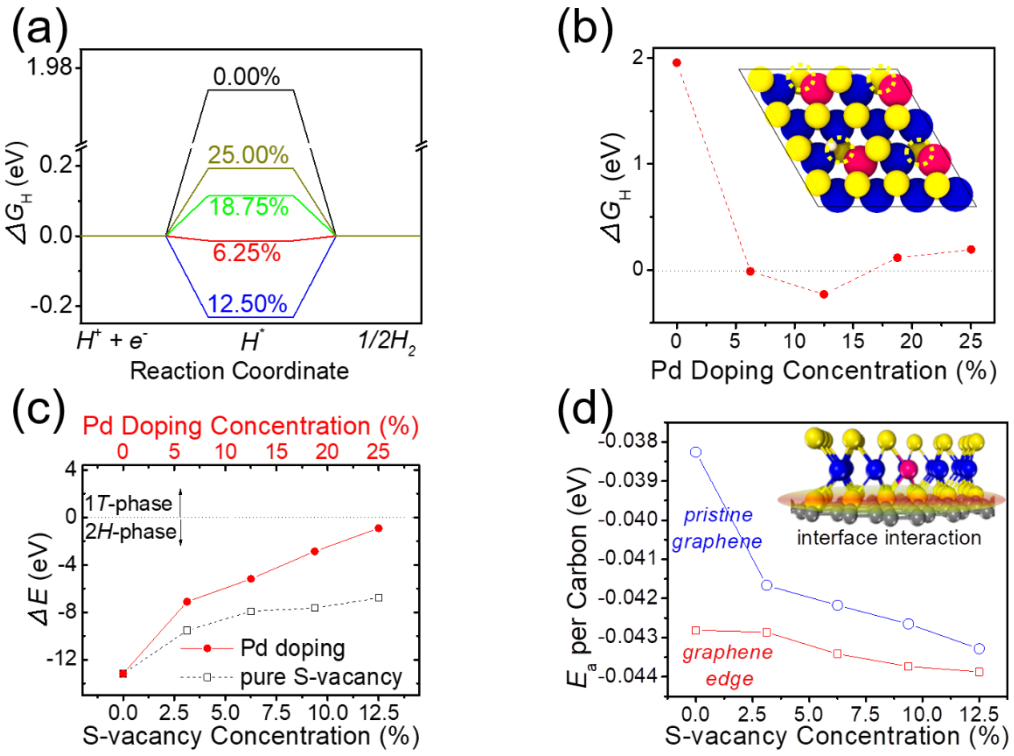

Fig. 5. Mechanism for enhanced activity and stability. (a) ΔG_H vs HER reaction coordinates. (b) hydrogen adsorption free energy ΔG_H as a function of Pd doping concentrations. Inset: atomic structure of hydrogen adsorbed on Pd-doped MoS_2 (25%). (c) The stability of 2*H*-phase at various concentration of Pd doping-induced (solid circles; upper x-axis) and pure S-vacancies (open squares; lower x-axis), respectively. 1*T* and 2*H* phases are labelled with the boundary at $\Delta E = 0$ eV. (d) Adsorption energy between catalyst and support (E_a) normalized to carbon atoms in graphene support (pristine graphene and graphene edge) as a function of S-vacancy percentages. Inset: schematic of enhanced catalyst-support interaction at the 2D-2D interface.

Next, we use DFT to examine the influence of Pd doping-induced S-vacancies on HER activity. By substituting Pd into MoS_2, Pd concentration becomes proportional to

the S-vacancy concentration. We assume that this process leads to the activation of the Pd-MoS_2 basal plane through the formation of S-vacancies. The hydrogen absorption free energy ΔG_H was employed as an indicator to evaluate HER activity (see Fig. 5a and Supplementary Fig. S8 for different simulation cases before and after H atom adsorption), where we measure ΔG_H primarily on the sulfur and sulfur-vacancy sites of Pd-MoS_2. Fig. 5b summarizes the dependence of ΔG on Pd doping concentration [see inset for the simulated unit cell where a hydrogen atom (white dot) adsorbs on one of the S-vacancy (dotted circle)]. The pristine MoS_2 without Pd doping or S-vacancy shows ΔG_H value of +1.97 eV, indicating the hydrogen adsorption on catalyst surface is unfavorable. Once Pd doping occurs (6.25%), sulfur vacancies are formed. Sulfur vacancy sites were found to have ΔG_H value of around -0.01 eV, indicating significantly enhanced hydrogen adsorption. Interestingly, ΔG_H value remains stable around ±0.2 eV from 6.25% to 25%, suggesting robust activity insensitive to Pd doping concentration in this range. This is consistent with the stable activity over 1000-h continuous operation when Pd concentration varies due to the dynamic catalyst surface during testing (Fig. S7). Additionally, the ΔG_H value close to zero also serves as good explanation for the excellent activity of VGN@Pd_x-MoS_2.

The robust stability can be attributed to the stable Pd_x-MoS_2 and the increased adhesion between catalyst and support due to S-vacancies. The relative energetic phase stability between the 2*H* and 1*T* structure (ΔE, see Method) was also evaluated, as depicted in Fig. 5c. It suggests that Pd doping-induced S-vacancies are stable in 2*H*-phase MoS_2 within 25% doping concentration, similar to the pure S-vacancy (*e.g.*,

plasma-induced). Previous studies have suggested support interactions from the hybridization of electronic states between MoS_2 layer and graphene with the formation of band gaps in the π-band of graphene.[53] And the defects in both MoS_2 and VGN can play crucial roles to form stable 2D heterostructure. We thus calculated the adsorption energy E_a between single 2D graphene layer of VGN and single 2D MoS_2 layer, as illustrated in Fig. 5d. Noting that all adhesions between MoS_2/graphene are exergonic, indicating minimum interface energy can be achieved by their hybrid, to stabilize MoS_2 on graphene layer. Furthermore, as the S-vacancy concentration increases, the adhesion between VGN and MoS_2 continuously enhanced. E_a increases by 10% when 3.125% S-vacancy (corresponding to 6.25% Pd doping) is created in MoS_2 supported on pristine graphene. This enhancement increases to 14% when 12.5% S-vacancy (corresponding to 25% Pd doping) is created, suggesting S-vacancy efficiently enhance the interaction between MoS_2 and graphene layers. We also calculated the adsorption energy of MoS_2 on defective graphene (C-defects) arising from mesoplasma deposition. A typical defect type of graphene, i.e., the edge (with most C-defects), was selected for calculating the adsorption interaction although many C-defects may exist on the VGN system such as 2 carbon atoms vacancies, an aromatic ring of 6 carbon vacancies as reported.[35] As shown in Fig. 5d, similar trend of enhanced adsorption as S-vacancy concentration increases appears despite the smaller enhancement obtained, because the MoS_2-graphene edge already shows good adhesion at 0% S-vacancy. These observations suggest that defects in VGN support effectively stabilize the catalyst structure by stronger interaction at the interface.

4. Conclusions

Ultrastable HER catalyst in acidic solution made from hybridizing MoS_2 with VGN and trace amount of Pd doping (<5 μg cm^{-2} that is 100-200 times lower than Pt loading in commercial PEM HER catalyst) has been demonstrated. VGN limited the growth of MoS_2 to form ultrathin layers, leading to large electrochemically active surface area and low Ohmic loss. Pd substitutional doping offered a facile and controllable technique to boost the activity of MoS_2. The catalysts have shown superior HER activities including low onset potential (-70 mV vs RHE) and small Tafel slope (60 mV/dec). Importantly, the catalyst exhibited a stable operation over 1000 h at 10 mA cm^{-2}, suggesting the great promise of the catalyst alternative to Pt-based HER catalyst for PEM water electrolysis that could be driven by intermittent renewable energies. DFT simulations detailed several possible pathways of the Pd substitutional doping process. Mo-vacancy formation is found to be the most energetically challenging step. Subsequent Pd atom substitution at the Mo site in all pathways was found to be facile. DFT simulation also revealed the optimization of hydrogen adsorption from Pd doping-induced sulfur vacancies. Moreover, the enhanced stability arising from the increased adhesion between doped MoS_2 and VGN support was also verified theoretically. Overall, from both experimental and theoretical aspects, this work offers a promising strategy for the design of cost-effective electrocatalyst with greatly enhanced stability.

Declaration of competing interest

The authors declare no competing financial interest.

Acknowledgements

The work was supported by Shell (China) Limited (award number PT78956). H.L. would like to thank Nanyang Technological University under NAP award (M408050000) and Tier 1 RG101/18 (2018-T1-001-051) for financial support.

Appendix A. Supplementary data

Supplementary data to this article can be found online at ……

References

[1] A. Ursua, L.M. Gandia, P. Sanchis, Hydrogen production from water electrolysis: current status and future trends. Proc. IEEE 100 (2011) 410-426.
[2] S. Chu, A. Majumdar, Opportunities and challenges for a sustainable energy future. Nature 488 (2012) 294.
[3] M.G. Walter, E.L. Warren, J.R. McKone, S.W. Boettcher, Q. Mi, E.A. Santori, N.S. Lewis, Solar water splitting cells. Chem. Rev. 110 (2010) 6446-6473.
[4] A.P. Murthy, J. Madhavan, K. Murugan, Recent advances in hydrogen evolution reaction catalysts on carbon/carbon-based supports in acid media. J. Power Sources 398 (2018) 9-26.
[5] J. Nowotny, C. Sorrell, L. Sheppard, T. Bak, Solar-hydrogen: environmentally safe fuel for the future. Int. J. Hydrogen Energy 30 (2005) 521-544.
[6] G. Notton, M.-L. Nivet, C. Voyant, C. Paoli, C. Darras, F. Motte, A. Fouilloy, Intermittent and stochastic character of renewable energy sources: Consequences, cost of intermittence and benefit of forecasting. Renewable Sustainable Energy Rev. 87 (2018) 96-105.
[7] M. Carmo, D.L. Fritz, J. Mergel, D. Stolten, A comprehensive review on PEM water electrolysis. Int. J. Hydrogen Energy 38 (2013) 4901-4934.
[8] V. Mehta, J.S. Cooper, Review and analysis of PEM fuel cell design and manufacturing. J. Power Sources 114 (2003) 32-53.
[9] B. Hinnemann, P.G. Moses, J. Bonde, K.P. Jørgensen, J.H. Nielsen, S. Horch, I. Chorkendorff, J.K. Nørskov, Biomimetic hydrogen evolution: MoS_2 nanoparticles as catalyst for hydrogen evolution. J. Am. Chem. Soc. 127 (2005) 5308-5309.
[10] T.F. Jaramillo, K.P. Jørgensen, J. Bonde, J.H. Nielsen, S. Horch, I. Chorkendorff, Identification of active edge sites for electrochemical H_2 evolution from MoS_2 nanocatalysts. Science 317 (2007) 100-102.
[11] M.A. Lukowski, A.S. Daniel, F. Meng, A. Forticaux, L. Li, S. Jin, Enhanced hydrogen evolution catalysis from chemically exfoliated metallic MoS_2 nanosheets. J. Am. Chem. Soc. 135 (2013) 10274-10277.
[12] H. Li, C. Tsai, A.L. Koh, L. Cai, A.W. Contryman, A.H. Fragapane, J. Zhao, H.S. Han, H.C. Manoharan, F. Abild-Pedersen, Activating and optimizing MoS_2 basal planes for hydrogen evolution through the formation of strained sulphur vacancies. Nat. Mater. 15 (2016) 48.
[13] Y. Yin, J. Han, Y. Zhang, X. Zhang, P. Xu, Q. Yuan, L. Samad, X. Wang, Y. Wang, Z. Zhang, Contributions of phase, sulfur vacancies, and edges to the hydrogen evolution reaction catalytic activity of porous molybdenum disulfide nanosheets. J. Am. Chem. Soc. 138 (2016) 7965-7972.
[14] J. Kibsgaard, Z. Chen, B.N. Reinecke, T.F. Jaramillo, Engineering the surface structure of MoS_2 to preferentially expose active edge sites for electrocatalysis. Nat. Mater. 11 (2012) 963.
[15] D. Voiry, M. Salehi, R. Silva, T. Fujita, M. Chen, T. Asefa, V.B. Shenoy, G. Eda, M. Chhowalla, Conducting MoS_2 nanosheets as catalysts for hydrogen evolution reaction. Nano Lett. 13 (2013) 6222-6227.

[16] H. Li, M. Du, M.J. Mleczko, A.L. Koh, Y. Nishi, E. Pop, A.J. Bard, X. Zheng, Kinetic study of hydrogen evolution reaction over strained MoS_2 with sulfur vacancies using scanning electrochemical microscopy. J. Am. Chem. Soc. 138 (2016) 5123-5129.
[17] K. Yu, D.J. Groom, X. Wang, Z. Yang, M. Gummalla, S.C. Ball, D.J. Myers, P.J. Ferreira, Degradation mechanisms of platinum nanoparticle catalysts in proton exchange membrane fuel cells: the role of particle size. Chem. Mater. 26 (2014) 5540-5548.
[18] B. Konkena, K. Junge Puring, I. Sinev, S. Piontek, O. Khavryuchenko, J.P. Dürholt, R. Schmid, H. Tüysüz, M. Muhler, W. Schuhmann, Pentlandite rocks as sustainable and stable efficient electrocatalysts for hydrogen generation. Nat. Commun. 7 (2016) 12269.
[19] J. Xiong, J. Li, J. Shi, X. Zhang, W. Cai, Z. Yang, H. Cheng, Metallic 1T-MoS_2 nanosheets in-situ entrenched on N, P, S-codoped hierarchical carbon microflower as an efficient and robust electro-catalyst for hydrogen evolution. Appl. Catal., B 243 (2019) 614-620.
[20] D.J. Li, U.N. Maiti, J. Lim, D.S. Choi, W.J. Lee, Y. Oh, G.Y. Lee, S.O. Kim, Molybdenum sulfide/N-doped CNT forest hybrid catalysts for high-performance hydrogen evolution reaction. Nano Lett. 14 (2014) 1228-1233.
[21] X. Zhang, X. Yu, L. Zhang, F. Zhou, Y. Liang, R. Wang, Molybdenum Phosphide/Carbon Nanotube Hybrids as pH-Universal Electrocatalysts for Hydrogen Evolution Reaction. Adv. Funct. Mater. 28 (2018) 1706523.
[22] H. Wang, Z. Lu, D. Kong, J. Sun, T.M. Hymel, Y. Cui, Electrochemical tuning of MoS_2 nanoparticles on three-dimensional substrate for efficient hydrogen evolution. ACS Nano 8 (2014) 4940-4947.
[23] Q. Ma, P.M. Odenthal, J. Mann, D. Le, C.S. Wang, Y. Zhu, T. Chen, D. Sun, K. Yamaguchi, T. Tran, Controlled argon beam-induced desulfurization of monolayer molybdenum disulfide. J. Phys.: Condens. Matter 25 (2013) 252201.
[24] C. Tsai, H. Li, S. Park, J. Park, H.S. Han, J.K. Nørskov, X. Zheng, F. Abild-Pedersen, Electrochemical generation of sulfur vacancies in the basal plane of MoS_2 for hydrogen evolution. Nat. Commun. 8 (2017) 15113.
[25] Z. Luo, Y. Ouyang, H. Zhang, M. Xiao, J. Ge, Z. Jiang, J. Wang, D. Tang, X. Cao, C. Liu, Chemically activating MoS_2 via spontaneous atomic palladium interfacial doping towards efficient hydrogen evolution. Nat. Commun. 9 (2018) 2120.
[26] W. Wu, C. Niu, C. Wei, Y. Jia, C. Li, Q. Xu, Activation of MoS_2 Basal Planes for Hydrogen Evolution by Zinc. Angew. Chem. 131 (2019) 2051-2055.
[27] J.D. Benck, T.R. Hellstern, J. Kibsgaard, P. Chakthranont, T.F. Jaramillo, Catalyzing the hydrogen evolution reaction (HER) with molybdenum sulfide nanomaterials. ACS Catal. 4 (2014) 3957-3971.
[28] G. Kresse, J. Furthmüller, Efficient iterative schemes for ab initio total-energy calculations using a plane-wave basis set. Phys. Rev. B 54 (1996) 11169.
[29] P.E. Blöchl, Projector augmented-wave method. Phys. Rev. B 50 (1994) 17953.
[30] J.P. Perdew, K. Burke, Y. Wang, Generalized gradient approximation for the exchange-correlation hole of a many-electron system. Phys. Rev. B 54 (1996) 16533.
[31] B. Hammer, L.B. Hansen, J.K. Nørskov, Improved adsorption energetics within

density-functional theory using revised Perdew-Burke-Ernzerhof functionals. Phys. Rev. B 59 (1999) 7413.
[32] S. Grimme, Semiempirical GGA-type density functional constructed with a long-range dispersion correction. J. Comput. Chem. 27 (2006) 1787-1799.
[33] W. Zhou, X. Zou, S. Najmaei, Z. Liu, Y. Shi, J. Kong, J. Lou, P.M. Ajayan, B.I. Yakobson, J.-C. Idrobo, Intrinsic structural defects in monolayer molybdenum disulfide. Nano Lett. 13 (2013) 2615-2622.
[34] J.K. Nørskov, T. Bligaard, A. Logadottir, J. Kitchin, J.G. Chen, S. Pandelov, U. Stimming, Trends in the exchange current for hydrogen evolution. J. Electrochem. Soc. 152 (2005) J23-J26.
[35] Y. Zhao, M.T. Tang, S. Wu, J. Geng, Z. Han, K. Chan, P. Gao, H. Li, Rational design of stable sulfur vacancies in molybdenum disulfide for hydrogen evolution. J. Catal. 382 (2020) 320-328.
[36] H.-U. Kim, M. Kim, Y. Jin, Y. Hyeon, K.S. Kim, B.-S. An, C.-W. Yang, V. Kanade, J.-Y. Moon, G.Y. Yeom, Low-temperature wafer-scale growth of MoS_2-graphene heterostructures. Appl. Surf. Sci. 470 (2019) 129-134.
[37] Y. Shi, W. Zhou, A. Lu, W. Fang, Y. Lee, A. Hsu, S.M. Kim, K. Kim, H. Yang, L. Li, J-C. Idrobo, and J. Kong, van der Waals Epitaxy of MoS_2 Layers Using Graphene As Growth Templates. Nano Lett 12 (2012) 2784-2791.
[38] N. Xue, P. Diao, Composite of few-layered MoS_2 grown on carbon black: tuning the ratio of terminal to total sulfur in MoS_2 for hydrogen evolution reaction. J. Phys. Chem. C 121 (2017) 14413-14425.
[39] H. Li, Q. Zhang, C.C.R. Yap, B.K. Tay, T.H.T. Edwin, A. Olivier, D. Baillargeat, From bulk to monolayer MoS_2: evolution of Raman scattering. Adv. Funct. Mater. 22 (2012) 1385-1390.
[40] H. Zhang, S. Wu, Z. Lu, X. Chen, Q. Chen, P. Gao, T. Yu, Z. Peng, J. Ye, Efficient and controllable growth of vertically oriented graphene nanosheets by mesoplasma chemical vapor deposition. Carbon 147 (2019) 341-347.
[41] H. Vrubel, D. Merki, X. Hu, Hydrogen evolution catalyzed by MoS_3 and MoS_2 particles. Energy Environ. Sci. 5 (2012) 6136-6144.
[42] B. Li, L. Jiang, X. Li, Z. Cheng, P. Ran, P. Zuo, L. Qu, J. Zhang, Y. Lu, Controllable Synthesis of Nanosized Amorphous MoS_x Using Temporally Shaped Femtosecond Laser for Highly Efficient Electrochemical Hydrogen Production. Adv. Funct. Mater. 29 (2019) 1806229.
[43] L.R.L. Ting, Y. Deng, L. Ma, Y.-J. Zhang, A.A. Peterson, B.S. Yeo, Catalytic activities of sulfur atoms in amorphous molybdenum sulfide for the electrochemical hydrogen evolution reaction. ACS Catal. 6 (2016) 861-867.
[44] Y. Yan, B. Xia, X. Ge, Z. Liu, J.-Y. Wang, X. Wang, Ultrathin MoS_2 nanoplates with rich active sites as highly efficient catalyst for hydrogen evolution. ACS Appl. Mater. Interfaces 5 (2013) 12794-12798.
[45] X. Zheng, J. Xu, K. Yan, H. Wang, Z. Wang, S. Yang, Space-confined growth of MoS_2 nanosheets within graphite: the layered hybrid of MoS_2 and graphene as an active catalyst for hydrogen evolution reaction. Chem. Mater. 26 (2014) 2344-2353.
[46] D. Albani, M. Shahrokhi, Z. Chen, S. Mitchell, R. Hauert, N. López, J. Pérez-

Ramírez, Selective ensembles in supported palladium sulfide nanoparticles for alkyne semi-hydrogenation. Nat. Commun. 9 (2018) 2634.
[47] X. Zhang, Z. Luo, P. Yu, Y. Cai, Y. Du, D. Wu, S. Gao, C. Tan, Z. Li, M. Ren, Lithiation-induced amorphization of $Pd_3P_2S_8$ for highly efficient hydrogen evolution. Nat. Catal. 1 (2018) 460-468.
[48] Y.-Y. Liu, H.-P. Zhang, B. Zhu, H.-W. Zhang, L.-D. Fan, X.-Y. Chai, Q.-L. Zhang, J.-H. Liu, C.-X. He, C/N-co-doped Pd coated Ag nanowires as a high-performance electrocatalyst for hydrogen evolution reaction. Electrochim. Acta 283 (2018) 221-227.
[49] X. Liu, I. Balla, H. Bergeron, M.C. Hersam, Point defects and grain boundaries in rotationally commensurate MoS_2 on epitaxial graphene. J. Phys. Chem. C 120 (2016) 20798-20805.
[50] S.A. Ghopry, M.A. Alamri, R. Goul, R. Sakidja, J.Z. Wu, Extraordinary Sensitivity of Surface-Enhanced Raman Spectroscopy of Molecules on MoS_2 (WS_2) Nanodomes/Graphene van der Waals Heterostructure Substrates. Adv. Opt. Mater. 7 (2019) 1801249.
[51] A. Azcatl, X. Qin, A. Prakash, C. Zhang, L. Cheng, Q. Wang, N. Lu, M.J. Kim, J. Kim, K. Cho, Covalent nitrogen doping and compressive strain in MoS_2 by remote N_2 plasma exposure. Nano Lett. 16 (2016) 5437-5443.
[52] L. Wu, A. Longo, N.Y. Dzade, A. Sharma, M.M. Hendrix, A.A. Bol, N.H. De Leeuw, E.J. Hensen, J.P. Hofmann, The Origin of High Activity of Amorphous MoS_2 in the Hydrogen Evolution Reaction. ChemSusChem 12 (2019) 1-8.
[53] H. Coy Diaz, J. Avila, C. Chen, R. Addou, M.C. Asensio, M. Batzill, Direct observation of interlayer hybridization and Dirac relativistic carriers in graphene/MoS_2 van der Waals heterostructures. Nano Lett. 15 (2015) 1135-1140.